ENVIRONMENTAL RESEARCH
LETTERS

LETTER • **OPEN ACCESS**

Contrasting impact of single-year and multi-year El Niño on the Pacific-North American teleconnection pattern

To cite this article: Yixuan Liu *et al* 2024 *Environ. Res. Lett.* **19** 124056

ENVIRONMENTAL RESEARCH
LETTERS

CrossMark

OPEN ACCESS

RECEIVED
1 August 2024

REVISED
7 November 2024

ACCEPTED FOR PUBLICATION
8 November 2024

PUBLISHED
19 November 2024

LETTER

Contrasting impact of single-year and multi-year El Niño on the Pacific-North American teleconnection pattern

Yixuan Liu[1,3], **Weichen Tao**[1,*], **Gang Huang**[1,2,3,*], **Ya Wang**[4,5,*], **Kaiming Hu**[1,5,6] and **Yong Liu**[6]

[1] State key Laboratory of Numerical Modeling for Atmospheric Sciences and Geophysical Fluid Dynamics (LASG), Institute of Atmospheric Physics, Chinese Academy of Sciences, Beijing, People's Republic of China
[2] Laboratory for Regional Oceanography and Numerical Modeling, Qingdao National Laboratory for Marine Science and Technology, Qingdao, People's Republic of China
[3] University of Chinese Academy of Sciences, Beijing, People's Republic of China
[4] Earth System Numerical Simulation Science Center, Institute of Atmospheric Physics, Chinese Academy of Sciences, Beijing, People's Republic of China
[5] Key Laboratory of Earth System Numerical Modeling and Application, Institute of Atmospheric Physics, Chinese Academy of Sciences, Beijing, People's Republic of China
[6] Center for Monsoon System Research, Institute of Atmospheric Physics, Chinese Academy of Sciences, Beijing, People's Republic of China
[*] Authors to whom any correspondence should be addressed.

E-mail: tao@mail.iap.ac.cn, hg@mail.iap.ac.cn and wangya@mail.iap.ac.cn

Keywords: Pacific-North American (PNA) teleconnection pattern, El Niño, Rossby wave source, subtropical jet stream (STJ), nonlinear energy advection, synoptic-scale transient eddy

Supplementary material for this article is available online

Abstract

Distinct Pacific-North American (PNA) teleconnection patterns and their associated climate impacts in North America have been observed during single-year El Niño events, as well as during both the first and second years of multi-year El Niño events. The research highlights the critical role of PNA-related North Pacific circulation anomalies, which shift northwestward during multi-year events and reach their peak intensity in the second year. Multiple dynamical diagnostic methods are employed to elucidate the reasons behind the diverse subtropical circulation responses. Differences in the anomalous tropical heat sources influence the formation of Rossby wave sources through adjustments in divergent wind anomalies, subsequently modulating the position and intensity of the PNA patterns. Additionally, variations in the meridional range of sea surface temperature anomalies affect the edge of tropospheric temperature through moist-adiabatic adjustment, leading to distinct subtropical jet stream responses. This, in turn, modifies the position of North Pacific circulation anomalies through the advection of anomalous kinetic energy. Furthermore, synoptic-scale transient eddies act as a feedback mechanism, helping to maintain and intensify these diverse atmospheric anomalies.

1. Introduction

The El Niño-Southern oscillation (ENSO) is the dominant mode of global climate variability on interannual time scales (Neelin *et al* 1998, Giese and Carton 1999, McPhaden *et al* 2006, Yeh *et al* 2018). The intricate evolution of ENSO exhibits multifaceted characteristics. For example, the El Niño and La Niña are the warm and cold phase of ENSO, respectively. During its developing phase, El Niño typically manifests with a stronger amplitude compared to La Niña (Burgers and Stephenson 1999, An and Jin 2004, Choi *et al* 2013, Dommenget *et al* 2013). This difference is tied to the robustness of the Bjerknes feedback loop, encompassing the sensitivity of wind stress to sea surface temperature (SST) anomalies, SST response to thermocline anomalies, and thermocline adjustment to wind stress anomalies, which are all more pronounced for El Niño than La Niña (Meinen and McPhaden 2000, Choi *et al* 2013, Timmermann *et al* 2018, Geng *et al* 2019). These complex properties can cause El Niño to end quickly and La Niña to persist (Larkin and Harrison 2002, Okumura and Deser 2010, Okumura *et al* 2011, Choi *et al* 2013), further affecting the diversity and asymmetry of El Niño and La Niña durations.

In terms of diversity, following an El Niño event, it is possible to shift to a La Niña state, a neutral state, or continue in an El Niño state in the subsequent year (Kessler 2002, Larkin and Harrison 2002, Tao *et al* 2017, 2022, Yu and Fang 2018, Fang and Yu 2020). As for asymmetry, La Niña is more prone to develop into a multi-year (MY) event, and El Niño predominantly spans a single year, although MY El Niño does occur. The disparity in ENSO duration is influenced by its own intensity, spatial distribution, pre-onset Pacific condition, as well as intricate inter-basin interactions (Vimont *et al* 2003, Tao *et al* 2018, Chakravorty *et al* 2020, Fang and Yu 2020, Ding *et al* 2022, Kim and Yu 2022, Iwakiri *et al* 2023, Kim *et al* 2023, Lin and Yu 2024, Wang *et al* 2024).

The global climate response to ENSO events varies depending on the durations of these events. Research on the climate impacts of MY ENSO events can be broadly classified into two categories: one focuses on comparing the climate difference between the first and second year of a MY event (Okumura *et al* 2017, Raj Deepak *et al* 2019, Jong *et al* 2020, Mamani Jimenez *et al* 2023, Huang *et al* 2024), and the other examines the contrasts between MY and single-year (SY) events (Mamani Jimenez *et al* 2023, Zhong *et al* 2023, Huang *et al* 2024). Although El Niño is more likely to manifest as a SY event compared to La Niña, numerous historical cases of MY El Niño events have been observed (Gao *et al* 2023). Most previous studies concentrated on MY La Niña events, and less attentions have been paid to MY El Niño events. However, impacts of MY El Niño events on the Pacific-North America (PNA) region not only differ from SY events but also exhibit distinct contrast between the first and second year as documented in the present study.

Tropical convective anomalies induced by ENSO trigger Rossby waves that propagate poleward across the PNA region, resulting in extreme weather and climate events in North America (Horel and Wallace 1981, Renwick and Wallace 1996, Hoerling *et al* 1997, Trenberth *et al* 1998, Okumura *et al* 2017). However, the PNA pattern is not identical in each ENSO event, for example, the asymmetrical circulation response between El Niño and La Niña, and multiple mechanisms has been proposed to explain this asymmetry. On one hand, the differences in tropical heating anomalies between El Niño and La Niña cause different divergent wind responses (Hoskins and Karoly 1981, Hoerling *et al* 1997, 2001, Alexander *et al* 2002), which influence the formation of Rossby wave source (RWS) thereby affect the wave trains (Sardeshmukh and Hoskins 1988). On the other hand, different zonally symmetric responses to ENSO, such as changes in tropical tropospheric temperature and the subtropical jet stream (STJ; Held *et al* 2002, Seager *et al* 2003) in both hemispheres, contribute to the asymmetric PNA teleconnection patterns through nonlinear energy advection. During El Niño events, the STJ tends to enhance and shift southward, while during La Niña events, it weakens and moves northward (Seager *et al* 2003, Lu *et al* 2008, Yang *et al* 2018, Wang *et al* 2021, 2022b). These changes redistribute the anomalous kinetic energy by nonlinear energy advection, leading to distinct PNA patterns (Simmons *et al* 1983, Wang *et al* 2022a, 2023). In addition, transient eddies responded to baroclinicity changes due to ENSO can help maintain the asymmetry as a feedback effect in the subtropical region (Hoskins *et al* 1983, Lau and Holopainen 1984, Trenberth 1986, Lau *et al* 2005). Given these complexities, it is essential to investigate the mechanisms driving the differences in PNA patterns between SY and MY El Niño events, as well as between the first and second year of MY El Niño events.

The remainder of this paper is structured as follows: the data and methods used are described in section 2. In section 3, we compare the differences of PNA teleconnection patterns among SY El Niño events and the first and second year of MY El Niño events, and provide possible explanations for these differences. Section 4 presents a summary and discussion.

2. Data and methods

2.1. Data

The monthly and daily-mean reanalysis datasets from the fifth generation of the European Centre for Medium-range Weather Forecasts (ERA5) are employed in this study, which include geopotential, wind, vertical velocity, total precipitation, air temperature, and 2 m air temperature (Muñoz Sabater 2019, Hersbach *et al* 2023a, 2023b, 2023c). The SST data is taken from the Hadley Centre Sea Ice and SST, version 1.1 (HadISSTv1.1; Rayner *et al* 2003). All data are selected for the 1950–2023 period and linearly detrended. Statistical significance of the composite anomalies is evaluated through a bootstrap test at the 90% confidence level.

2.2. Identifying SY and MY El Niño events

SY and MY El Niño events are selected based on the monthly SST anomalies averaged in the Niño3.4 region (5° S–5° N, 120°–170° W). If the October–November–December–January–February (ONDJF) mean Niño3.4 index of an El Niño event is greater than 0.5 standard deviations in the first year and also greater than 0.5 standard deviations in the second year, then it is a MY El Niño event (Geng *et al* 2023). 14 SY El Niño events (1951/52, 1957/58, 1963/64, 1965/66, 1972/73, 1979/80, 1982/83, 1991/92, 1994/95, 1997/98, 2002/03, 2004/05, 2006/07, 2009/10) and 5 MY El Niño events (1968/70, 1976/78, 1986/88, 2014/16, 2018/20) are identified from 1950 to 2023. Hereafter, suffix (0) refers to the developing year of SY events and the first developing year of MY events, and suffix (+1) is the second developing year of MY events.

2.3. RWS

To understand the influence of El Niño on subtropical atmospheric circulation, the RWS is diagnosed, which is derived from the barotropic vorticity equation (Sardeshmukh and Hoskins 1988). Following Sekizawa *et al* (2021), the RWS can be calculated as follows:

$$
\begin{aligned}
RWS' &= -\nabla\cdot(\boldsymbol{V}_\chi\zeta)' \\
&\approx -\bar{\zeta}\nabla\cdot\boldsymbol{V}_\chi{}' - \boldsymbol{V}_\chi{}'\cdot\nabla\bar{\zeta} - \zeta'\nabla\cdot\overline{\boldsymbol{V}_\chi} \\
&\quad - \overline{\boldsymbol{V}_\chi}\cdot\nabla\zeta'
\end{aligned}
\tag{1}
$$

where $\boldsymbol{V}_\chi$ denotes divergent wind and ζ the absolute vorticity, the prime signifies an anomaly, the overbar signifies a climatological-mean quantity. The first term ($-\bar{\zeta}\nabla\cdot\boldsymbol{V}_\chi{}'$), representing the stretching effect by anomalous divergence acting on the climatological absolute vorticity, is the dominant term of equation (1). This implies that in regions where the climatological absolute vorticity is significant, the presence of anomalous convergence or divergence can lead to the development of vorticity, thereby stimulating the formation of Rossby waves.

2.4. Eddy kinetic energy tendency equation

Following Wang *et al* (2023), the complete eddy kinetic energy tendency equation can be calculated as follows:

$$
\begin{aligned}
\frac{\partial EKE}{\partial t} = & \underbrace{-\left[u'^2\frac{\partial\bar{u}}{\partial x} + u'v'\left(\frac{\partial\bar{u}}{\partial y}+\frac{\partial\bar{v}}{\partial x}\right) + v'^2\frac{\partial\bar{v}}{\partial y} + u'\omega'\frac{\partial\bar{u}}{\partial p} + v'\omega'\frac{\partial\bar{v}}{\partial p}\right]}_{\mathrm{KI}} \\
& \underbrace{-(u'+\bar{u})\left(\frac{\partial EKE}{\partial x}\right) - (v'+\bar{v})\left(\frac{\partial EKE}{\partial y}\right) - (\omega'+\bar{\omega})\left(\frac{\partial EKE}{\partial p}\right)}_{\mathrm{KA}} \\
& \underbrace{-\frac{R}{P}\omega'T'}_{\mathrm{KP}} \underbrace{-u'\frac{\partial\phi'}{\partial x} - v'\frac{\partial\phi'}{\partial y} - \omega'\frac{\partial\phi'}{\partial p}}_{\mathrm{KZ}}
\end{aligned}
\tag{2}
$$

where *EKE* is the eddy kinetic energy, u', v', ω', T' and ϕ' are the anomalous monthly zonal wind, meridional wind, vertical wind, temperature, and geopotential, respectively, $\bar{u}$ and $\bar{v}$ represent the background zonal and meridional flow. KI represents the kinetic energy extracted from the basic flow, while the conversion from anomalous effective potential energy to anomalous kinetic energy is represented by KP. The combination of KP and KI forms as the energy source of the disturbance. KA describes the kinetic energy advected by the basic flow and the anomalous wind, which could be seen as the redistribution term. This term could be further decomposed to linear KA ($\mathrm{lKA} = -[\bar{u}\frac{\partial EKE}{\partial x} + \bar{v}\frac{\partial EKE}{\partial y} + \bar{\omega}\frac{\partial EKE}{\partial p}]$) and nonlinear KA ($\mathrm{nKA} = -[u'\frac{\partial EKE}{\partial x} + v'\frac{\partial EKE}{\partial y} + \omega'\frac{\partial EKE}{\partial p}]$). The generation of the *EKE* by local convergence of the eddy geopotential flux is given by KZ.

2.5. Geopotential height tendency and Eliassen-Palm vectors

To analyze the interaction between synoptic-scale transient eddies and the wave train, we use the geopotential height tendency and Eliassen–Palm vectors (hereafter referred to as $\boldsymbol{E}$ vectors). Following Lau *et al* (2005), they can be calculated as follows:

$$
\left(\frac{\partial Z}{\partial t}\right)_{eddy} = \frac{f}{g}\nabla^{-2}\left[-\nabla\cdot\left(\overline{\boldsymbol{V}''\zeta''}\right)\right] \tag{3}
$$

$$
\boldsymbol{E} = \frac{1}{2}\left(\overline{v''^2} - \overline{u''^2}\right)\boldsymbol{i} - \overline{v''u''}\boldsymbol{j} \tag{4}
$$

where Z is the monthly averaged geopotential height, g is the acceleration of gravity, and $\boldsymbol{V}''$, u'', v'' and ζ'' are the synoptic-scale daily 200 hPa winds and relative vorticity. The high frequency components are all filtered by a band of 2.5–8 days and the overbar represents the monthly average.

3. Results

3.1. Atmospheric circulations induced by SY and MY El Niño events

Figure 1 shows the DJF composite anomalies of 200 hPa geopotential height during SY events and the first and second year of MY events. The PNA teleconnection patterns are evident in all three cases, with variations in their distribution and intensity. In the tropical segment of the PNA patterns, the circulation anomalies in SY events are more eastward-shifted and stronger compared to MY events. Among the three cases, MY (0) exhibits the most westward and weakest circulation anomalies, whereas MY (+1) presents intermediate characteristics in both location and

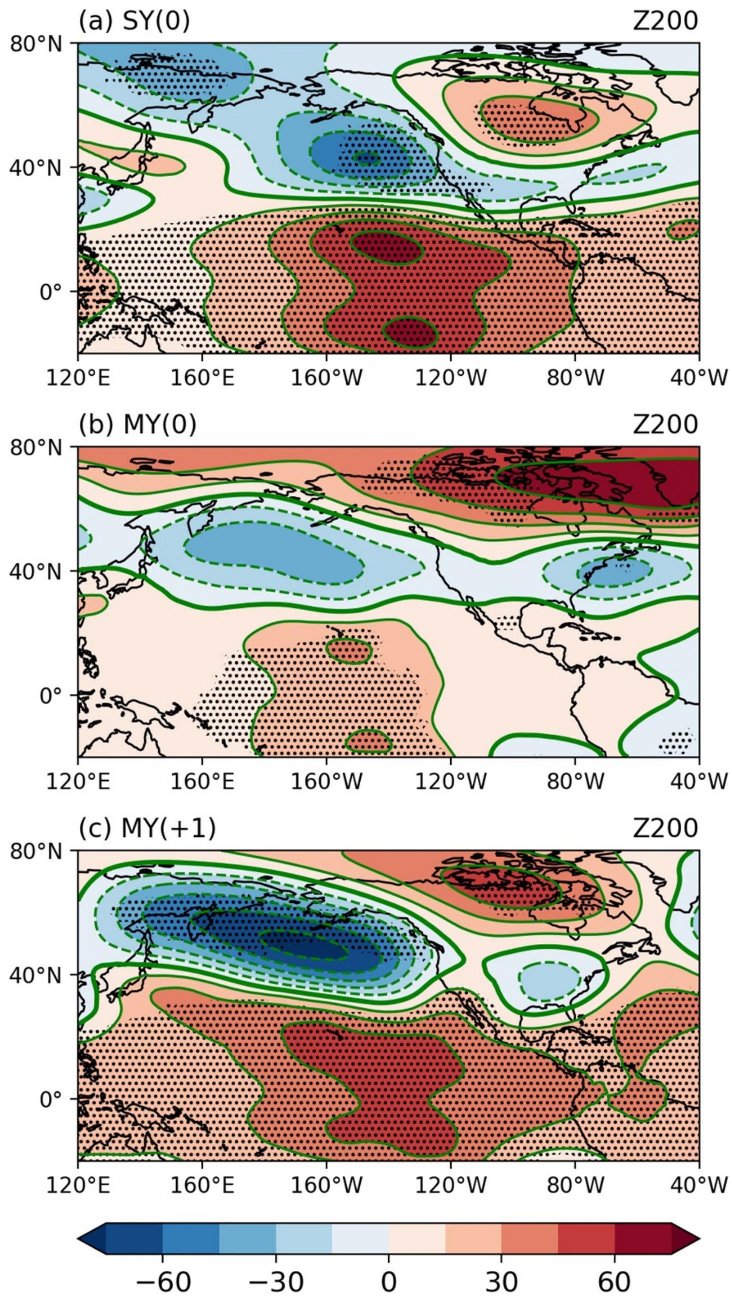

Figure 1. DJF composite of 200 hPa geopotential height (m) anomalies during (a) SY (0), (b) MY (0) and (c) MY (+1). Black dots indicate the statistically significant anomalies at the 90% confidence level.

intensity between SY and MY (0). Correspondingly, the SST and precipitation anomalies in the tropical Pacific reflect consistent spatial distribution and intensity patterns across the three cases (figure 2), and they induce the differences in tropical circulation anomalies by triggering a Rossby wave response (figure 1). Composite analyses show that while the SSTA for SY and MY events resemble those for Eastern Pacific (EP) and Central Pacific (CP) El Niño, which are part of a widely recognized ENSO classification (Ashok *et al* 2007, Kao and Yu 2009, Kug *et al* 2009, Yeh *et al* 2009, Tao *et al* 2014), the Z200 distribution differs significantly (figures S1(a)–S1(d)). SY and MY El Niño events do not directly correspond to EP and CP El Niño events (figure S1(e)).

In the North Pacific region, the zonal positions of negative geopotential height anomalies among the three cases generally mirror the characteristics of positive geopotential height anomalies in the tropics, with a more westward shift in MY (0) and MY (+1) than in SY (figure 1). Additionally, the circulation anomalies during MY (0) and MY (+1) move more northward than those during SY in meridional locations. However, the subtropical circulation anomalies across the three cases display inconsistent intensity characteristics compared to the tropical

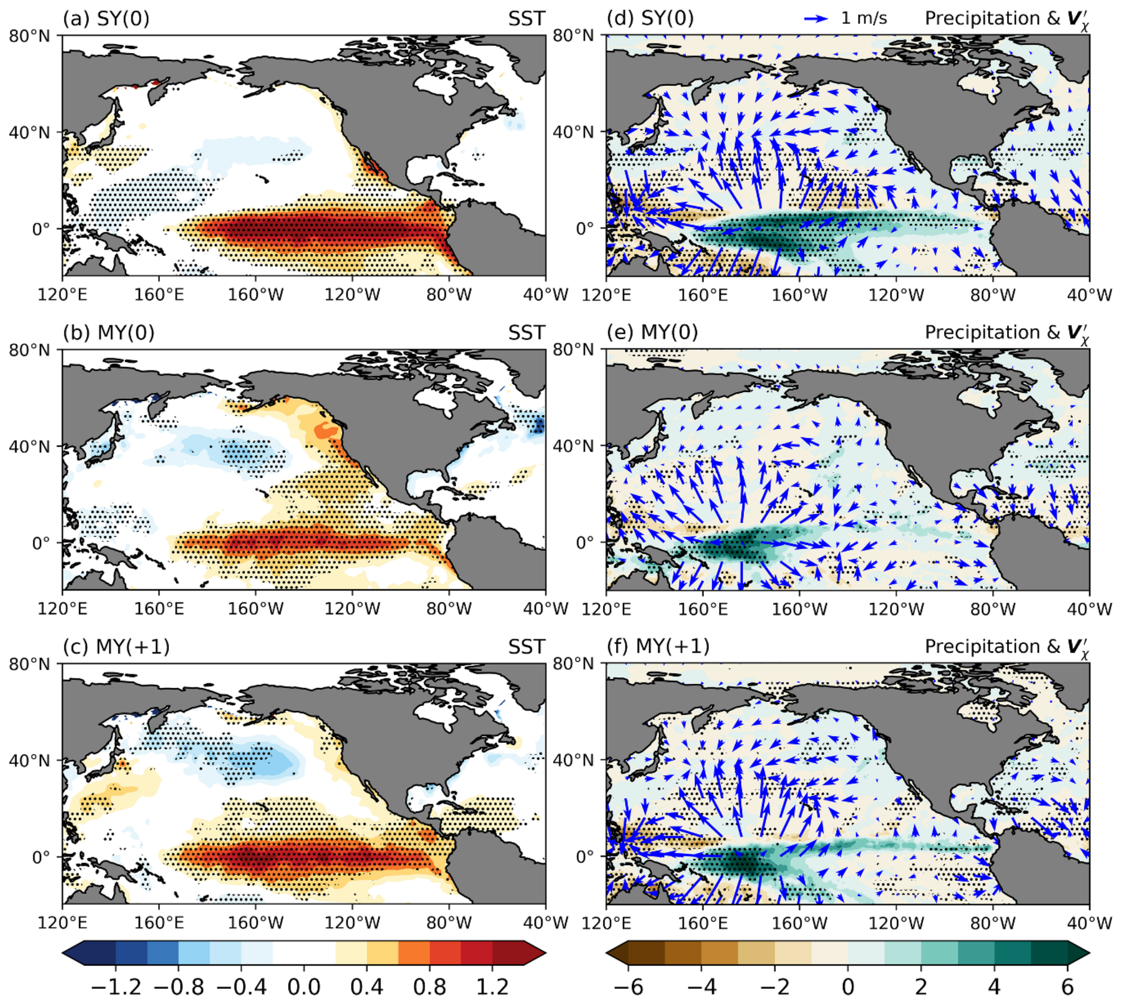

Figure 2. DJF composite of (a)–(c) SST (°C) and (d)–(f) precipitation (shading; m) and $V_\chi{}'$ (vector; m s^{-1}) anomalies during (a), (d) SY (0), (b), (e) MY (0) and (c), (f) MY (+1), respectively. Black dots indicate the statistically significant anomalies at the 90% confidence level.

circulation anomalies. While MY (+1) exhibits intermediate intensity of tropical circulation anomalies between SY and MY (0), it shows the strongest subtropical circulation anomalies. The PNA-related North Pacific circulation anomalies in MY (0) do not reach statistical significance, which could be attributed to the small sample size of MY events and the weak and diverse tropical heat sources in MY (0) (figures not shown).

For the North American segment of PNA patterns, the positive geopotential height anomalies in MY events are slightly stronger compared to SY events (figure 1). The circulation anomalies over North America in MY events are positioned more northwestward than SY events, following the similar distribution patterns observed in subtropical circulation anomalies. Note that the circulation anomalies in MY (0) shift eastward to southern Greenland with a wide zonal extension. Further analysis of the 500 hPa geopotential height anomalies reveals the presence of two independent cells over North America and southern Greenland, respectively (figure S2(b)), and they merge into one cell at 200 hPa (figure 1(b)). The western cell is associated with PNA pattern, while the eastern cell, along with the anomalous low height counterpart to its south, closely resembles the North Atlantic Oscillation pattern (Wallace and Gutzler 1981). The positional differences of regional positive geopotential height anomalies lead to corresponding differences of the high temperature areas in North America, with anomalies in SY (MY) events situated south (north) of 60° N (figure S3).

As previously mentioned, the North American segment of PNA pattern is largely influenced by its tropical and subtropical counterparts. Tropical circulation anomalies are a direct response to heating anomalies in the tropics. Subtropical circulation anomalies in the North Pacific link the tropical and North America segment of PNA pattern, affected by both tropical processes and intricate atmospheric dynamics in the subtropics (Simmons *et al* 1983, Hoerling *et al* 1997, Seager *et al* 2010, Okumura *et al* 2017, Wang *et al* 2023, Wang and Yang 2023, Gan *et al* 2024). Thus, elucidating the reasons in the differences

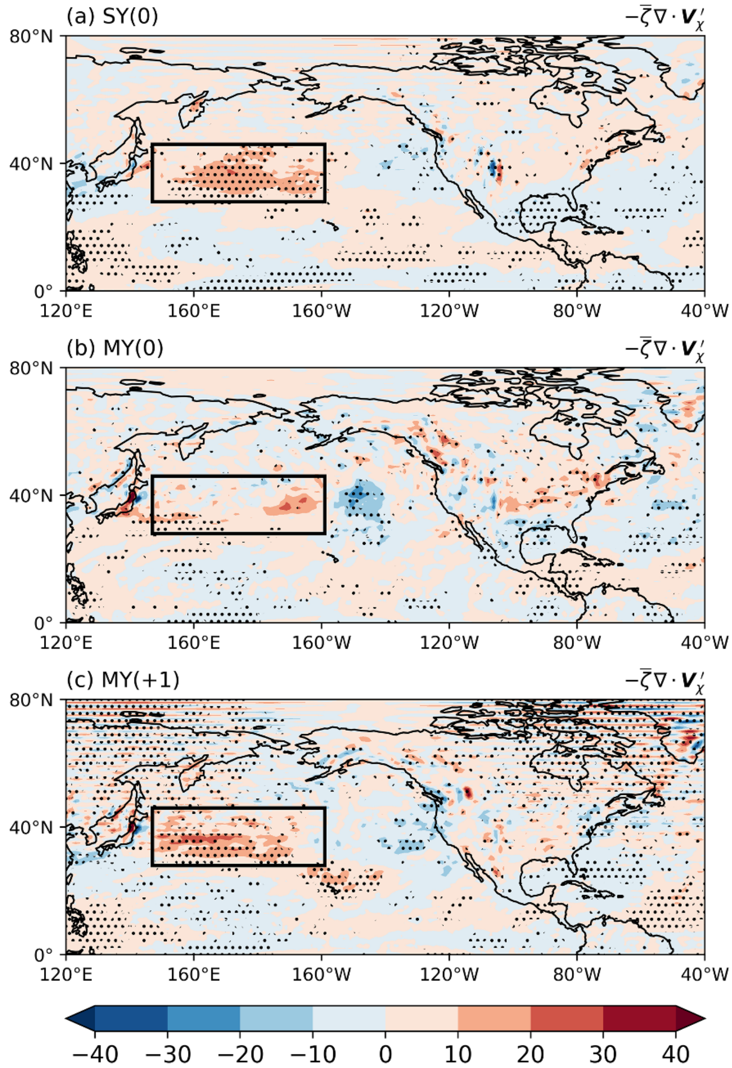

Figure 3. DJF composite of the main term of RWS ($-\bar{\zeta}\nabla\cdot\boldsymbol{V}_\chi{}'$) (shading; 10^{-11} s^{-2}) during (a) SY (0), (b) MY (0) and (c) MY (+1). Black dots indicate the statistically significant anomalies at the 90% confidence level.

of circulation anomalies in the North Pacific among the three cases is important to understand the diverse PNA responses to El Niño events, and this will be explored in the following subsections.

3.2. The role of RWS

Tropical SST anomalies induce convergent and divergent winds, which, in conjunction with suitable background circulation, generate RWS in the subtropics. These sources affect atmospheric circulation anomalies by exciting steady Rossby waves. According to the decomposition of equation (1), the magnitude of $-\bar{\zeta}\nabla\cdot\boldsymbol{V}_\chi{}'$ is on the same scale as RWS with a nearly identical distribution (figures 3 and S4) and is significantly larger than the other three terms (figures 3 and S5), which emerges as the primary contributor to RWS. Given that the climatological STJ is located around 30° N and positive vorticity forms at its north side (figures 5(a)–(c)), the positive RWS generally concentrates along 40° N in the North Pacific accompanied with anomalous convergent winds originated from the tropics (figure S4). The positive area of $-\bar{\zeta}\nabla\cdot\boldsymbol{V}_\chi{}'$ in SY (0) is located further east than that in MY (+1) (figure 3), attributing to the eastward displacement of the tropical heat source and the resulting tropical divergence and subtropical convergence anomalies in SY events (figures 2(d) and (f)). Then, the positional difference of RWS influences the origin position of the wave trains, contributing to the difference in the zonal positions of PNA-related North Pacific circulation anomalies between SY (0) and MY (+1). In addition, the intensity of $-\bar{\zeta}\nabla\cdot\boldsymbol{V}_\chi{}'$ in the North Pacific during MY (+1) is stronger than during SY (0) (figure 3), which explains the intensity difference in circulation anomalies between these two cases. This difference is attributed to the strength of tropical precipitation anomalies and the resulting subtropical divergent wind anomalies (figures 2(d) and (f)). The distribution of the positive area of $-\bar{\zeta}\nabla\cdot\boldsymbol{V}_\chi{}'$ in MY

(0) differs from the other two cases (figure 3). The positive-value areas are scattered, with both narrow meridional and zonal ranges, and most areas are occupied by weak positive values. This distribution does not effectively enhance the development of the wave trains, resulting in the circulation anomalies over the North Pacific in MY (0) being significantly weaker than in the other two cases. The above analysis emphasizes the critical role of the difference in tropical heat anomalies, which modulate both the position and intensity of RWS and thereby contribute to the difference in North Pacific circulation anomalies among the three cases.

3.3. The role of zonally symmetric response

The Pacific STJ exit zone, characterized by confluent zonal winds, promotes kinetic energy conversion from mean flow and facilitates the development of North Pacific circulation anomalies (Simmons *et al* 1983, Wang *et al* 2021, 2023). Influenced by tropical heat sources, changes in the intensity and spatial structure of the STJ can adjust the position of circulation anomalies by redistributing subtropical atmospheric kinetic energy through the nonlinear energy advection (Hoerling *et al* 1997, Wang *et al* 2021). Equation (2) is employed to diagnose the dominant term of eddy kinetic energy around the North Pacific among the three cases, and the distribution of each term are shown in figure S6. KI and KA have large magnitude, and lKA closely approximates the value of KA. The climatological zonal flow remains consistent across the three cases, and KI and lKA generate different patterns based on the distinct circulation anomalies. Similarly, the spatial distribution of KZ corresponds well to the North Pacific circulation anomalies among three cases, and the different KZ patterns are the result of circulation anomalies rather than the underlying cause. Hence, none of these terms can be identified as the primary driver of the PNA-related circulation anomalies over the North Pacific (Wang *et al* 2023). In comparison to the other terms, the value of KP is relatively small and lacks a clear distribution pattern, which may be attributed to the quasi-barotropic structure of the PNA pattern (Horel and Wallace 1981, Wallace and Gutzler 1981, Held *et al* 2002). Wang *et al* (2023) demonstrated that nKA plays a crucial role in driving the asymmetric PNA pattern during El Niño and La Niña events. They further noted that, as the anomalies in nKA consist of both zonal flow and wave trains, $\mathrm{nKA\_}\langle u\rangle = -\langle u'\rangle \frac{\partial EKE}{\partial x}$ (where $\langle u'\rangle$ represents the zonal mean zonal flow anomaly) displays a similar pattern to nKA. Moreover, the difference in $\mathrm{nKA\_}\langle u\rangle$ distribution can well explain the difference in the position of the North Pacific circulation anomalies related to PNA teleconnection pattern.

Figure 4 shows the distribution of $\mathrm{nKA\_}\langle u\rangle$ during SY (0), MY (0) and MY (+1). Consistent with Wang *et al* (2023), $\mathrm{nKA\_}\langle u\rangle$ is crucial for nKA (figures 4 and S6), and it exhibits a zonal dipole distribution along 20–40° N in the North Pacific, featuring a 'west negative and east positive' structure in the three cases. However, this zonal dipole distribution shifts more southeastward in SY events than MY events. Compared to MY events, the STJ is more significantly strengthened and moves more southward in SY events (figures 5(a)–(c)). The strengthened (southward) STJ favors a more eastward (southward)-shifted 'west negative and east positive' $\mathrm{nKA\_}\langle u\rangle$ distribution, resulting in the circulation disturbances developing further east (south) (figures 1 and 4). It is important to note that the role of STJ and resultant nKA are emphasized to contribute the positional difference of North Pacific circulation anomalies rather than intensity difference.

The meridional gradient of tropospheric temperature closely links to STJ following thermal wind balance. The edge of tropospheric temperature warming in SY events is located around 20° N (figure 5(d)), corresponding well with nearby strengthened upper-level westerlies (figure 5(a)). In contrast, the edge extends to 35° N in MY events, and the meridional gradient of tropospheric temperature anomalies is weaker compared to SY events (figures 5(e) and (f)), accompanied by the poleward shift and moderate enhancement of the STJ (figures 5(b) and (c)). Furthermore, the meridional differences in tropospheric temperature anomalies originate from differences in meridional range of SST anomalies through moist-adiabatic adjustment (Su and Neelin 2003, Xie *et al* 2009, Tandon *et al* 2013, Yang *et al* 2020). Significant SST warming occurs within 10° S–10° N of the deep tropics in SY events, whereas the zonal mean SST profile in MY events covers a broader range and the SST warming can extend up to 30° N (figures 5(g) and S7), thereby leading to the distinct tropospheric temperature and STJ responses among the three cases (figures 5(a)–(f)).

3.4. The role of synoptic-scale transient eddy

In addition to the roles of RWS and STJ, synoptic-scale transient eddies play a significant role in maintaining the differences in circulation anomalies through a feedback effect (Hu *et al* 2018, Wang *et al* 2023). Figure 6 shows the distribution of composite geopotential height tendency and ***E*** vectors induced by synoptic-scale transient eddies during SY (0), MY (0) and MY (+1). Moreover, the Eady growth rate (EGR; Vallis 2017) is calculated to measure the relationship between stationary wave train and eddy activities, and it is given by $\sigma_E = 0.3098\frac{|f|\left|\frac{\partial u}{\partial z}\right|}{N}$, where

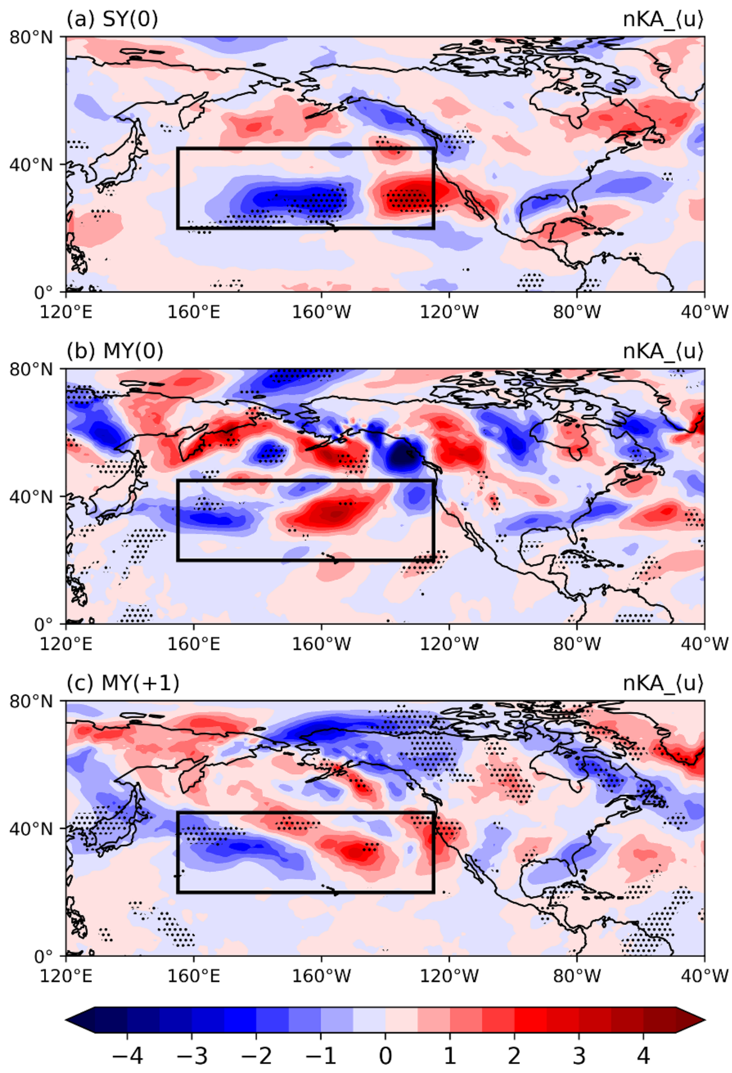

Figure 4. Horizontal distribution of composite nKA_$\langle u \rangle$ (10^{-5} m^2 s^{-3}) during (a) SY (0), (b) MY (0) and (c) MY (+1). Black dots indicate the statistically significant anomalies at the 90% confidence level.

N is the Brunt–Väisälä frequency, $N^2 = \frac{g}{\theta}\frac{\partial \theta}{\partial z}$, g is the acceleration due to gravity, θ is the potential temperature, and f is the Coriolis parameter. In all three cases, the stationary wave train enhances vertical wind shear and baroclinic instability in the North Pacific region (figures 1 and S8(a)–(c)), leading to the increased synoptic-scale eddy activities (figures S8(d)–(f)), and negative eddy-induced geopotential height tendency anomalies consistently appear in this region (figure 6). The increased eddy activities correspond with the divergence of $\boldsymbol{E}$ vectors at 40° N, accelerating the upper-level westerlies in the southern part of the negative geopotential height anomalies (figures 1 and 6), which, in turn, further contributes to the enhancement of baroclinic instability (figure S8). This positive feedback mechanism sustains and amplifies the circulation anomalies over the North Pacific, resulting in the differences of circulation anomalies among the three cases. During MY events, the divergence area of the $\boldsymbol{E}$ vectors extends further northwestward, corresponding to a more northwestward shift of negative geopotential height anomalies in the North Pacific than SY events (figures 1 and 6). Note that the negative geopotential height tendency anomalies during MY (+1) extend to North America, which exhibits positive eddy-induced geopotential height tendency anomalies during MY (0) (figures 6(b) and (c)). This may partially explain why the PNA teleconnection pattern during MY (+1) is stronger in both the tropics and the North Pacific, but not as strong as that during MY (0) in North America (figures 1(b) and (c)).

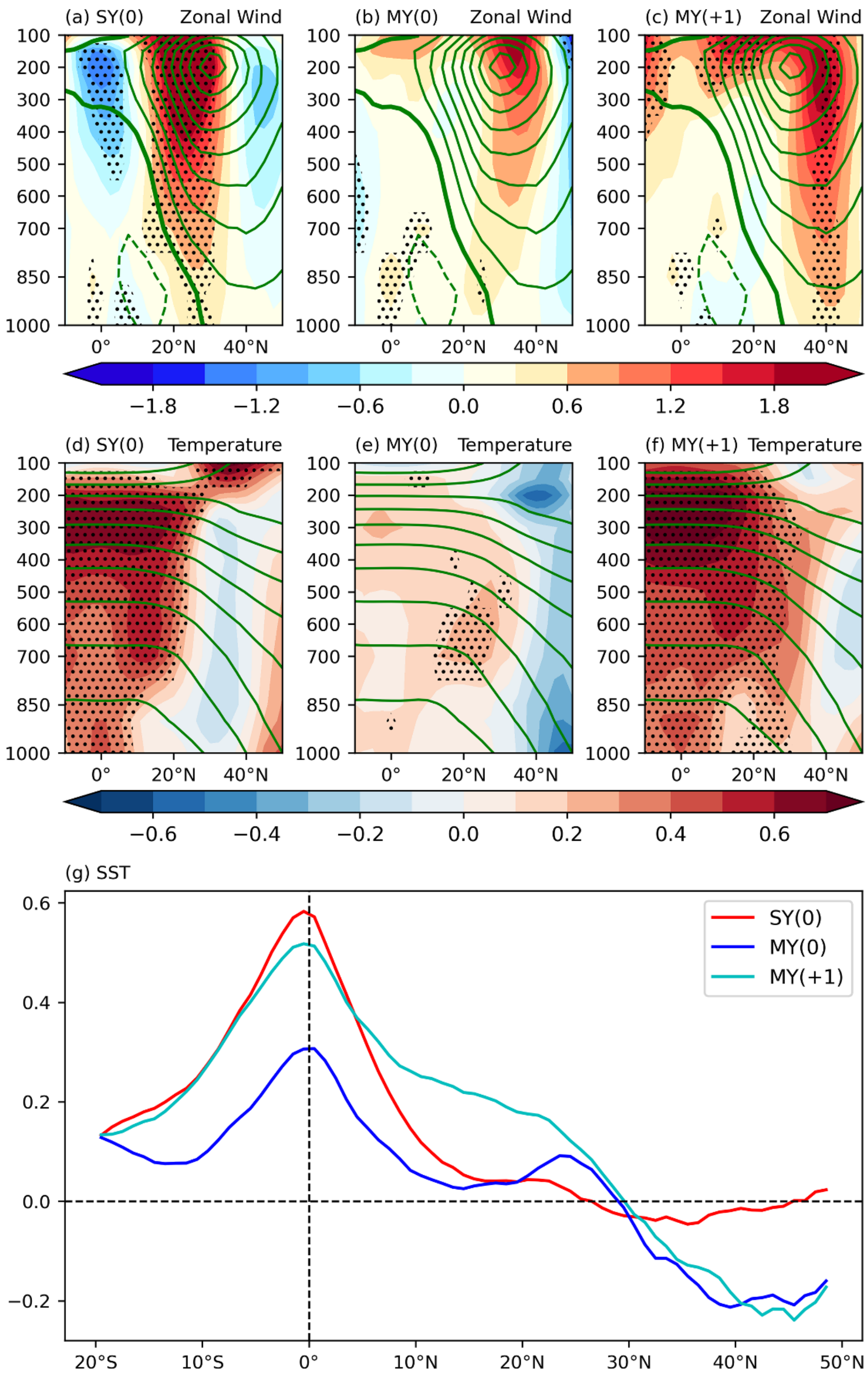

Figure 5. Composite DJF zonal mean (a)–(c) zonal wind (m s^{-1}) and (d)–(f) temperature (K) anomalies during (a), (d) SY (0), (b), (e) MY (0) and (c), (f) MY (+1). Contour lines denote the climatology. Zonal mean (g) SST (°C) anomalies during SY (0) (red line), MY (0) (blue line) and MY (+1) (cyan line). Black dots indicate the statistically significant anomalies at the 90% confidence level.

4. Conclusion and discussion

Based on a composite analysis of observational and reanalysis data, distinct PNA teleconnection patterns and their climate impacts in North America are observed during SY El Niño events and the first and second year of MY El Niño events. This study emphasizes the critical role of subtropical circulation anomalies in the North Pacific for linking the tropical and North America segment of the PNA pattern. In terms of position, the subtropical circulation anomalies in the North Pacific shift more northwestward during MY events compared to SY events. Regarding intensity, the negative geopotential

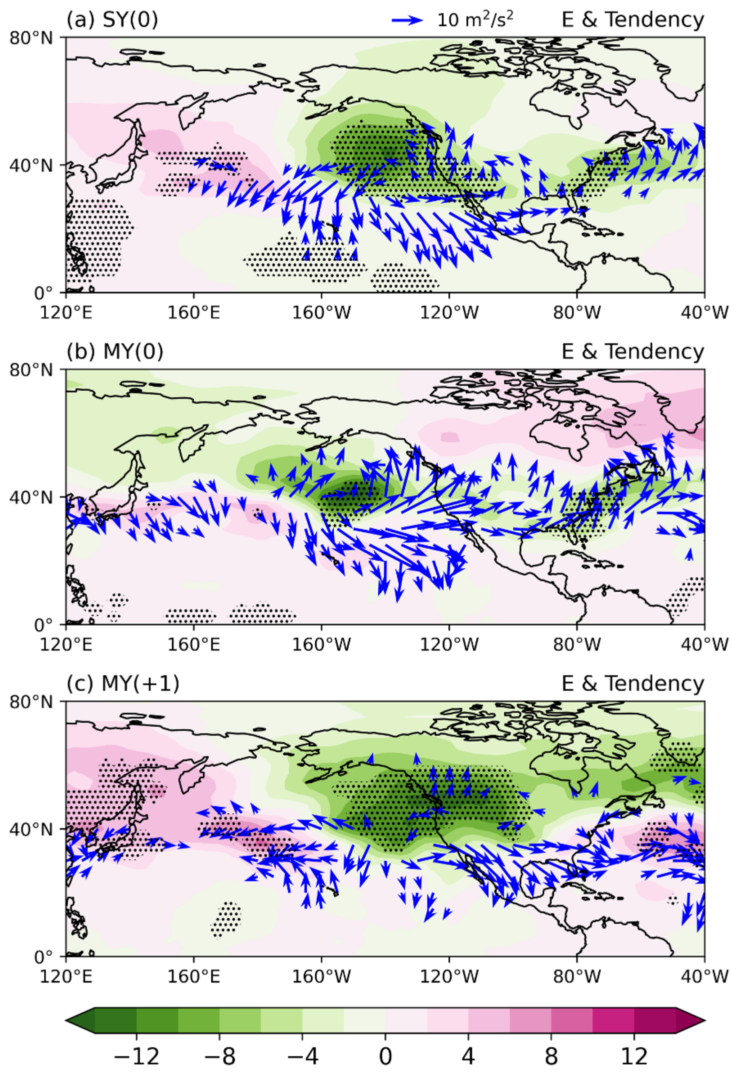

Figure 6. Horizontal distribution of composite geopotential height tendency (shading; m/day) and Eliassen-Palm ***E*** vectors (vector; $m^2\ s^{-2}$) during (a) SY (0), (b) MY (0) and (c) MY (+1). The ***E*** vectors with magnitudes smaller than 4 $m^2 s^{-2}$ are not plotted. Black dots indicate the statistically significant anomalies at the 90% confidence level.

height anomalies in MY (+1) are stronger than those in MY (0).

Multiple dynamical diagnostic methods are employed to elucidate the reasons behind the diverse subtropical circulation response among the three cases. From the perspective of tropical origin, the pivotal role of the ENSO-induced tropical heat source is confirmed. The differences in anomalous tropical heat sources influence the formation of RWS through adjustments of divergent wind anomalies, subsequently modulating the position and intensity of the PNA patterns. Consistent with the spatial distribution of tropical heat sources, the location of positive RWS in MY events is more westward than SY events, and the positive RWS in MY (+1) exhibits the strongest intensity.

From the perspective of subtropical processes, the STJ modifies the position of North Pacific circulation anomalies through the redistribution of subtropical atmospheric energy advection. nKA_$\langle u \rangle$ plays a primary role in this process, featuring a zonal dipole distribution with the 'west negative and east positive' structure along 20–40° N in the North Pacific across the three cases. During SY events, the more strengthened and southward-shifted STJ facilitates southeastward movement of nKA_$\langle u \rangle$, resulting in a more southeastward shift of North Pacific circulation anomalies compared to MY events. The diverse STJ response in the three cases originate from differences in meridional range of SST anomalies. Significant SST warming occurs within the deep tropics in SY events, whereas the zonal mean SST profile in MY events exhibits a broader meridional range, influencing the edge of tropospheric temperature through moist-adiabatic adjustment and thereby leading to distinct STJ responses among the three cases. Additionally, synoptic-scale transient eddies can affect North Pacific circulation anomalies as a positive feedback mechanism. In conclusion, RWS, STJ and synoptic-scale transient eddies jointly contribute to the positional differences, and the intensity differences can be interpreted by RWS.

Given that El Niño events typically persist for one year and develop into SY El Niño events, the number of observed MY El Niño events is limited. To ensure the robustness of the conclusions obtained in present study, we extend the starting time of study period to 1900. The merged ECMWF reanalysis dataset comprises the ERA-20C reanalysis for the period of 1900–1939 (Poli *et al* 2016) and the ERA5 reanalysis for the period of 1940–2023 (Hersbach *et al* 2023b). The differences between the ERA-20C and ERA5 datasets in monthly climatology during the overlap period 1940–2010 are calculated to calibrate the mean state of ERA-20C to ensure temporal consistency of these two datasets. Consequently, the number of MY El Niño events increases to 7, and there are 20 SY El Niño events. Figure S9 presents the DJF composite anomalies of 200 hPa geopotential height with the dataset extended to 1900–2023. The overall anomaly distribution highly resembles figure 1, except that the North Pacific circulation anomalies during MY (0) slightly shift southward. This shift is attributed to the relative meridionally narrow subtropical SST warming during MY (0) in the extended dataset (figure S10(g)), consequently moving the edge of tropospheric temperature (figure S10(e)) and the STJ southward (figure S10(b)).

Another important issue not addressed in the present study is that the PNA pattern, as an internal pattern of atmospheric variability in the Northern Hemisphere, can exist in the absence of tropical SST forcing, which is known as the venerable PNA pattern. Previous studies suggested that the PNA patterns induced by ENSO are different from those associated with internal variability (Straus and Shukla 2002, Lopez and Kirtman 2019). Other argue that ENSO forcing can only amplify the effects of internal variability and cannot generate a new PNA pattern (Palmer 1999). Therefore, further understanding of the specific influence of internal atmospheric variability, through model experiments or by separating external forcing from internal variability, is critical for more comprehensively considering the sources of these differences in the PNA pattern.

Data availability statement

The data that support the findings of this study are openly available at the following URL/DOI: The HadISSTv1.1 dataset is available at www.metoffice.gov.uk/hadobs/hadisst (Rayner *et al* 2003). The ERA5 hourly and monthly data on pressure levels are available at https://doi.org/10.24381/cds.bd0915c6 (Hersbach *et al* 2023a) and https://doi.org/10.24381/cds.6860a573 (Hersbach *et al* 2023b). The ERA5 global and land monthly data on single level are available at https://doi.org/10.24381/cds.f17050d7 (Hersbach *et al* 2023c) and https://doi.org/10.24381/cds.68d2bb30 (Muñoz Sabater 2019). The ERA-20C data can be obtained from www.ecmwf.int (Poli *et al* 2016).

Acknowledgment

This work is supported by the National Natural Science Foundation of China (Grant Nos. 42141019, 42261144687, 42475048, 42175049, and 42405041).

ORCID iDs

Yixuan Liu https://orcid.org/0009-0004-8248-2687
Weichen Tao https://orcid.org/0000-0002-4629-576X
Gang Huang https://orcid.org/0000-0002-8692-7856
Ya Wang https://orcid.org/0000-0003-1527-5413
Kaiming Hu https://orcid.org/0000-0002-9988-5747

References

Alexander M A, Bladé I, Newman M, Lanzante J R, Lau N and Scott J D 2002 The atmospheric bridge: the influence of ENSO teleconnections on air–sea interaction over the global oceans *J. Clim.* **15** 2205–31
An S-I and Jin F-F 2004 Nonlinearity and asymmetry of ENSO *J. Clim.* **17** 2399–412
Ashok K, Behera S K, Rao S A, Weng H and Yamagata T 2007 El Niño Modoki and its possible teleconnection *J. Geophys. Res.* **112** C11007
Burgers G and Stephenson D B 1999 The "normality" of El Niño *Geophys. Res. Lett.* **26** 1027–30
Chakravorty S, Perez R C, Anderson B T, Giese B S, Larson S M and Pivotti V 2020 Testing the trade wind charging mechanism and its influence on ENSO variability *J. Clim.* **33** 7391–411
Choi K, Vecchi G A and Wittenberg A T 2013 ENSO transition, duration, and amplitude asymmetries: role of the nonlinear wind stress coupling in a conceptual model *J. Clim.* **26** 9462–76
Ding R *et al* 2022 Multi-year El Niño events tied to the North Pacific Oscillation *Nat. Commun.* **13** 3871
Dommenget D, Bayr T and Frauen C 2013 Analysis of the non-linearity in the pattern and time evolution of El Niño southern oscillation *Clim. Dyn.* **40** 2825–47
Fang S-W and Yu J-Y 2020 Contrasting transition complexity between El Niño and La Niña: observations and CMIP5/6 models *Geophys. Res. Lett.* **47** e2020GL088926
Gan R, Huang G and Hu K 2024 The diverse impacts of El Niño on Northeastern Canada and Greenland surface air temperatures *J. Clim.* **37** 335–48
Gao Z, Hu Z-Z, Zheng F, Li X, Li S and Zhang B 2023 Single-year and double-year El Niños *Clim. Dyn.* **60** 2235–43
Geng T, Cai W, Wu L and Yang Y 2019 Atmospheric convection dominates genesis of ENSO asymmetry *Geophys. Res. Lett.* **46** 8387–96
Geng T, Jia F, Cai W, Wu L, Gan B, Jing Z, Li S and McPhaden M J 2023 Increased occurrences of consecutive La Niña events under global warming *Nature* **619** 774–81
Giese B S and Carton J A 1999 Interannual and decadal variability in the tropical and midlatitude Pacific Ocean *J. Clim.* **12** 3402–18

Held I M, Ting M F and Wang H L 2002 Northern winter stationary waves: theory and modeling *J. Clim.* **15** 2125–44

Hersbach H *et al* 2023a ERA5 hourly data on pressure levels from 1940 to present *Copernicus Climate Change Service (C3S) Climate Data Store (CDS)* (https://doi.org/10.24381/cds.bd0915c6)

Hersbach H *et al* 2023b ERA5 monthly averaged data on pressure levels from 1940 to present *Copernicus Climate Change Service (C3S) Climate Data Store (CDS)* (https://doi.org/10.24381/cds.6860a573)

Hersbach H *et al* 2023c ERA5 monthly averaged data on single levels from 1940 to present *Copernicus Climate Change Service (C3S) Climate Data Store (CDS)* (https://doi.org/10.24381/cds.f17050d7)

Hoerling M P, Kumar A and Xu T 2001 Robustness of the nonlinear climate response to ENSO's extreme phases *J. Clim.* **14** 1277–93

Hoerling M P, Kumar A and Zhong M 1997 El Niño, La Niña, and the nonlinearity of their teleconnections *J. Clim.* **10** 1769–86

Horel J D and Wallace J M 1981 Planetary-scale atmospheric phenomena associated with the southern oscillation *Mon. Weather Rev.* **109** 813–29

Hoskins B J, James I and White G H 1983 The shape, propagation and mean-flow interaction of large-scale weather systems *J. Atmos. Sci.* **40** 1595–612

Hoskins B J and Karoly D J 1981 The steady linear response of a spherical atmosphere to thermal and orographic *J. Atmos. Sci.* **38** 1179–96

Hu K, Huang G, Wu R and Wang L 2018 Structure and dynamics of a wave train along the wintertime Asian jet and its impact on East Asian climate *Clim. Dyn.* **51** 4123–37

Huang A T, Gillett Z E and Taschetto A S 2024 Australian rainfall increases during multi-year La Niña *Geophys. Res. Lett.* **51** e2023GL106939

Iwakiri T, Imada Y, Takaya Y, Kataoka T, Tatebe H and Watanabe M 2023 Triple-dip La Niña in 2020–23: north Pacific atmosphere drives 2nd year La Niña *Geophys. Res. Lett.* **50** e2023GL105763

Jong B, Ting M, Seager R and Anderson W B 2020 ENSO teleconnections and impacts on U.S. Summertime temperature during a multiyear La Niña life cycle *J. Clim.* **33** 6009–24

Kao H-Y and Yu J-Y 2009 Contrasting Eastern-Pacific and Central-Pacific types of ENSO *J. Clim.* **22** 615–32

Kessler W S 2002 Is ENSO a cycle or a series of events? *Geophys. Res. Lett.* **29** 2125

Kim J-W and Yu J-Y 2022 Single- and multi-year ENSO events controlled by pantropical climate interactions *npj Clim. Atmos. Sci.* **5** 88

Kim J-W, Yu J-Y and Tian B 2023 Overemphasized role of preceding strong El Niño in generating multi-year La Niña events *Nat. Commun.* **14** 6790

Kug J-S, Jin F-F and An S-I 2009 Two types of El Niño events: cold tongue El Niño and warm pool El Niño *J. Clim.* **22** 1499–515

Larkin N K and Harrison D E 2002 ENSO warm (El Niño) and cold (La Niña) event life cycles: ocean surface anomaly patterns, their symmetries, asymmetries, and implications *J. Clim.* **15** 1118–40

Lau N and Holopainen E O 1984 Transient eddy forcing of the time-mean flow as identified by geopotential tendencies *J. Atmos. Sci.* **41** 313–28

Lau N, Leetmaa A, Nath M J and Wang H 2005 Influences of ENSO-induced Indo-Western Pacific SST anomalies on extratropical atmospheric variability during the boreal summer *J. Clim.* **18** 2922–42

Lin Y-F and Yu J-Y 2024 The role of the Indian ocean in controlling the formation of multiyear El Niños through subtropical ENSO dynamics *J. Clim.* **37** 385–401

Lopez H and Kirtman B P 2019 ENSO influence over the Pacific North American sector: uncertainty due to atmospheric internal variability *Clim. Dyn.* **52** 6149–72

Lu J, Chen G and Frierson D M W 2008 Response of the zonal mean atmospheric circulation to El Niño versus global warming *J. Clim.* **21** 5835–51

Mamani Jimenez L C, Andreoli R V, Kayano M T, de Souza R A F and Ceron W L 2023 Multiyear versus single-year El Niño events: contrasting their impacts on South American seasonal precipitation *Int. J. Climatol.* **43** 6368–82

McPhaden M J, Zebiak S E and Glantz M H 2006 ENSO as an integrating concept in Earth science *Science* **314** 1740–5

Meinen C S and McPhaden M J 2000 Observations of warm water volume changes in the equatorial pacific and their relationship to El Niño and La Niña *J. Clim.* **13** 3551–9

Muñoz Sabater J 2019 ERA5-Land monthly averaged data from 1950 to present *Copernicus Climate Change Service (C3S) Climate Data Store (CDS)* (https://doi.org/10.24381/cds.68d2bb30)

Neelin J D, Battisti D S, Hirst A C, Jin F-F, Wakata Y, Yamagata T and Zebiak S E 1998 ENSO theory *J. Geophys. Res.* **103** 14261–90

Okumura Y M and Deser C 2010 Asymmetry in the duration of El Niño and La Niña *J. Clim.* **23** 5826–43

Okumura Y M, DiNezio P and Deser C 2017 Evolving impacts of multiyear La Niña events on atmospheric circulation and U.S. drought *Geophys. Res. Lett.* **44** 11614–23

Okumura Y M, Ohba M, Deser C and Ueda H 2011 A proposed mechanism for the asymmetric duration of El Niño and La Niña *J. Clim.* **24** 3822–9

Palmer T N 1999 A nonlinear dynamical perspective on climate prediction *J. Clim.* **12** 575–91

Poli P, Hersbach H, Dee D P, Berrisford P, Simmons A J and Vitart F 2016 ERA-20C: an atmospheric reanalysis of the twentieth century *J. Clim.* **29** 4083–97

Raj Deepak S N, Chowdary J S, Dandi A R, Srinivas G, Parekh A, Gnanaseelan C and Yadav R K 2019 Impact of multiyear La Niña events on the South and East Asian summer monsoon rainfall in observations and CMIP5 models *Clim. Dyn.* **52** 6989–7011

Rayner N A, Parker D E, Horton E B, Folland C K, Alexander L V, Rowell D P, Kent E C and Kaplan A 2003 Global analyses of sea surface temperature, sea ice, and night marine air temperature since the late nineteenth century *J. Geophys. Res.* **108** 4407

Renwick J A and Wallace J M 1996 Relationships between North Pacific wintertime blocking, El Niño, and the PNA pattern *Mon. Weather Rev.* **124** 2071–6

Sardeshmukh P D and Hoskins B J 1988 The generation of global rotational flow by steady idealized tropical divergence *J. Atmos. Sci.* **45** 1228–51

Seager R, Harnik N, Kushnir Y, Robinson W and Miller J 2003 Mechanisms of hemispherically symmetric climate variability *J. Clim.* **16** 2960–78

Seager R, Naik N, Ting M, Cane M A, Harnik N and Kushnir Y 2010 Adjustment of the atmospheric circulation to tropical Pacific SST anomalies: variability of transient eddy propagation in the Pacific–North America sector *Q. J. R. Meteorol. Soc.* **136** 277–96

Sekizawa S, Nakamura H and Kosaka Y 2021 Remote influence of the interannual variability of the Australian summer monsoon on wintertime climate in East Asia and the Western North Pacific *J. Clim.* **34** 9551–70

Simmons A J, Wallace J M and Branstator G W 1983 Barotropic wave-propagation and instability, and atmospheric teleconnection patterns *J. Atmos. Sci.* **40** 1363–92

Straus D M and Shukla J 2002 Does ENSO force the PNA? *J. Clim.* **15** 2340–58

Su H and Neelin J D 2003 The scatter in tropical average precipitation anomalies *J. Clim.* **16** 3966–77

Tandon N F, Gerber E P, Sobel A H and Polvani L M 2013 Understanding Hadley cell expansion versus contraction: insights from simplified models and implications for recent observations *J. Clim.* **26** 4304–21

Tao W, Huang G, Hu K, Qu X, Wen G and Gong Y 2014 Different influences of two types of El Niños on the Indian Ocean SST variations *Theor. Appl. Climatol.* **117** 475–84

Tao W, Huang G, Wu R, Hu K, Wang P and Chen D 2017 Asymmetry in summertime atmospheric circulation anomalies over the northwest Pacific during decaying phase of El Niño and La Niña *Clim. Dyn.* **49** 2007–23

Tao W, Huang G, Wu R, Hu K, Wang P and Gong H 2018 Origins of Biases in CMIP5 models simulating northwest pacific summertime atmospheric circulation anomalies during the decaying phase of ENSO *J. Clim.* **31** 5707–29

Tao W, Kong X, Liu Y, Wang Y and Dong D 2022 Diversity of Northwest Pacific atmospheric circulation anomalies during post-ENSO summer *Front. Environ. Sci.* **10** 1068155

Timmermann A *et al* 2018 El Niño–Southern Oscillation complexity *Nature* **559** 535–45

Trenberth K E 1986 An assessment of the impact of transient eddies on the zonal flow during a blocking episode using localized Eliassen-Palm flux *J. Atmos. Sci.* **43** 2070–87

Trenberth K E, Branstator G W, Karoly D, Kumar A, Lau N-C and Ropelewski C 1998 Progress during TOGA in understanding and modeling global teleconnections associated with tropical sea surface temperatures *J. Geophys. Res.* **103** 14291–324

Vallis G K 2017 *Atmospheric and Oceanic Fluid Dynamics* (Cambridge University Press)

Vimont D J, Wallace J M and Battisti D S 2003 The seasonal footprinting mechanism in the Pacific: implications for ENSO *J. Clim.* **16** 2668–75

Wallace J M and Gutzler D S 1981 Teleconnections in the geopotential height field during the Northern Hemisphere winter *Mon. Weather Rev.* **109** 784–812

Wang X and Yang X-Q 2023 Amplified asymmetric impact of ENSO events on the wintertime Pacific-North American teleconnection pattern *Geophys. Res. Lett.* **50** e2022GL100996

Wang Y, Hu K, Huang G and Tao W 2021 Asymmetric impacts of El Nino and La Nina on the Pacific-North American teleconnection pattern: the role of subtropical jet stream *Environ. Res. Lett.* **16** 114040

Wang Y, Hu K, Huang G and Tao W 2023 The role of nonlinear energy advection in forming asymmetric structure of ENSO teleconnections over the North Pacific and North America *Geophys. Res. Lett.* **50** e2023GL105277

Wang Y, Huang G, Hu K, Tao W, Gong H, Yang K and Tang H 2022a Understanding the eastward shift and intensification of the ENSO teleconnection over South Pacific and Antarctica under greenhouse warming *Front. Earth Sci.* **10** 916624

Wang Y, Huang G, Hu K, Tao W, Li X, Gong H, Gu L and Zhang W 2022b Asymmetric Impacts of El Niño and La Niña on the Pacific–South America teleconnection pattern *J. Clim.* **35** 1825–38

Wang Y, Huang G, Pan B, Lin P, Boers N, Tao W, Chen Y, Liu B and Li H 2024 Correcting climate model sea surface temperature simulations with generative adversarial networks: climatology, interannual variability, and extremes *Adv. Atmos. Sci.* **41** 1299–312

Xie S, Hu K, Hafner J, Tokinaga H, Du Y, Huang G and Sampe T 2009 Indian Ocean Capacitor effect on Indo–Western Pacific Climate during the summer following El Niño *J. Clim.* **22** 730–47

Yang H, Lohmann G, Lu J, Gowan E J, Shi X, Liu J and Wang Q 2020 Tropical expansion driven by poleward advancing midlatitude meridional temperature gradients *J. Geophys. Res.* **125** e2020JD033158

Yang S, Li Z, Yu J-Y, Hu X, Dong W and He S 2018 El Niño–Southern oscillation and its impact in the changing climate *Natl Sci. Rev.* **5** 840–57

Yeh S-W *et al* 2018 ENSO atmospheric teleconnections and their response to greenhouse gas forcing *Rev. Geophys.* **56** 185–206

Yeh S-W, Kug J-S, Dewitte B, Kwon M-H, Kirtman B P and Jin F-F 2009 El Niño in a changing climate *Nature* **461** 511–4

Yu J-Y and Fang S-W 2018 The distinct contributions of the seasonal footprinting and charged-discharged mechanisms to ENSO complexity *Geophys. Res. Lett.* **45** 6611–8

Zhong W, Wu Y, Yang S, Ma T, Cai Q and Liu Q 2023 Heavy southern China spring rainfall promoted by multi-year El Niño events *Geophys. Res. Lett.* **50** e2022GL102346